Article

Optimization of In Situ Formation of a Titanium Carbide Nanohybrid via Mechanical Alloying Using Stearic Acid and Carbon Nanotubes as Carbon Sources

María Luisa Camacho-Ríos [1,2,*], Guillermo Herrera-Pérez [3], Marco Antonio Ruiz Esparza-Rodríguez [2], Raúl Pérez-Bustamante [1], John Edison García-Herrera [4], José Antonio Betancourt-Cantera [1] and Daniel Lardizábal-Gutiérrez [2]

1   Corporación Mexicana de Investigación en Materiales S.A. de C.V. (COMIMSA), Ciencia y Tecnología 790, Saltillo 400, Saltillo 25290, Mexico; raul.perez@comimsa.com (R.P.-B.); jbetancourt@comimsa.com (J.A.B.-C.)
2   Centro de Investigación en Materiales Avanzados (CIMAV), Miguel de Cervantes 120, Chihuahua 31109, Mexico; marco.ruiz@cimav.edu.mx (M.A.R.E.-R.); daniel.lardizabal@cimav.edu.mx (D.L.-G.)
3   CONAHCYT-Centro de Investigación en Materiales Avanzados (CIMAV), Miguel de Cervantes 120, Chihuahua 31109, Mexico; guillermo.herrera@cimav.edu.mx
4   CONAHCYT-CIATEQ A.C. Centro de Tecnología Avanzada, Eje 126 No.225, Industrial San Luis, San Luis Potosi 78395, Mexico; john.garcia@ciateq.mx
*   Correspondence: luisa.camacho@cimav.edu.mx

Abstract: The current work shows the optimization of the preparation of nanosized titanium carbide in situ through mechanical alloying. Metallic titanium powders, along with two carbon sources, carbon nanotubes, and stearic acid, were used to reduce the particle size (around 11 nm) using an SPEX 800 high-energy mill. The combined use of 2 wt % of these carbon sources and n-heptane as a liquid process control agent proved crucial in generating nanoscale powder composites through a simple and scalable synthesis process within a 4 h timeframe. The uses of 20 wt % of both carbon sources were compared to determine the ability of carbon nanotubes to form carbides and the decomposition of process control agent during mechanical milling. The structure of the composites and starting materials were evaluated through X-ray diffraction and Raman spectroscopy, while the morphology features (average particle size and shape) were monitored via scanning electron microscopy and transmission electron microscopy.

Keywords: titanium carbide; nanocomposites; mechanical alloying; process control agent; carbon nanotubes; titanium

1. Introduction

Titanium carbide (TiC) is characterized as one of the metal carbides with high hardness (28–35 GPa), a high melting point (3067–3340 °C), great resistance to abrasion, a high chemical stability, thermal conductivity, and electrical conductivity [1]. TiC is commonly used as a reinforcement in other materials, such as aluminum, titanium, and their alloys [2,3]. In recent years, various synthesis methods have been studied, including carbo-thermal reduction, electrospinning, high-temperature self-propagation (SHS), and chemical vapor deposition [4,5]. This is because its production requires high temperatures, incurring high costs and prompting the industry to explore different alternatives.

Mechanical alloying is a method that allows the synthesis of materials with different properties, resulting in alloys that are stronger and lighter, making them attractive for the aerospace and automotive industries that demand such materials [6]. The steps in this method are optimized, eliminating the need for subsequent washes or heat treatments. TiC synthesis begins with elemental materials, Ti powders, and different carbon sources, such as graphite, CNTs, activated carbon, etc. [7,8]. The goal is to control the microstructure, design

the composites, distribute the carbon source in the metal matrix, and achieve chemical interaction, allowing the metal to wet the graphite and form carbides.

The formation of TiC is an exothermic process, and the phase is synthesized layer by layer through combustion or thermal explosion [9]. In the synthesis process through MA, organic surfactants or process control agents (PCAs) are used as lubricants to achieve a balance between material fracture and cold welding, improving the process efficiency and preventing the powder agglomeration resulting from milling. Nouri et al, in 2013 [10], conducted a study on the effect of PCAs in the mechanical milling process. They describe that there are solid and liquid PCAs, with the most commonly used being stearic acid (SA), ethylene bis stearamide (BIS), ethanol, methanol, hexane, oleic acid, etc. PCAs are absorbed onto the surface of particles, and during MA, they decompose into carbon, hydrogen, oxygen, and nitrogen. The combination of these elements with milling materials can lead to the formation of carbides, hydrides, oxides, and nitrides.

The decomposition of the PCA can be considered beneficial in various studies when the intention is to reduce the metallic oxides [11,12]. Another commonly reported decomposition of a PCA is that of carbon [13,14]. The reaction of metals with liquid PCAs derived from hydrocarbons such as hexane and n-heptane has been studied to evaluate their effect on particle size reduction. In both studies, the XRD results revealed the appearance of peaks corresponding to the formation of a new phase, suggesting that chemical reactivity increases during milling, favoring the transition of metals with carbon in carbide formation [15,16]. The decomposition of PCA by milling offers the dual advantage of being a tool that allows in situ carbide formation and a reduction of the particle size in the nanometric range.

Various strategies have been developed to improve the preparation of TiC using the ball milling method, as Lohse et al. [8] reported previously. These authors suggest that the high-energy ball milling method is considered the most effective method. To date, different kinds of ball milling, such as conventional ball milling, planetary ball milling, agate ball milling, vibratory mill, magneto ball milling, and SPEX, have been attempted. Liu et al. [17] report the preparation of $Ti_{100-x}C_x$ (where x = 35, 43, and 50) with milling times of 186, 179, and 140 min using an SPEX mill. Ye and Quan [18] prepared $Ti_{50}C_{50}$ using a planetary ball mill for 5 h. Shaffer and Forrester [19] prepared the same composition using a steel SPEX mill. These previous reports indicate that TiC can be produced via milling elemental titanium and carbon powder mixtures. In addition, Lohse et al. [8] suggest that the key points for the in situ fabrication of $Ti_{100-x}C_x$, are the composition, long milling time, and ball milling type. These parameters play an important role in reducing the particle size in the nanometer range for TiC. Therefore, there are ongoing efforts to explore facile in situ TiC preparation with the reduction of the particle size in the nanometer range (around 15 nm or less), considering a combination of these parameters with the use of a high-energy ball mill method.

The motivation for this work is to prepare in situ TiC composites using the mechanical alloying technique (within a 4 h timeframe) to reduce the particle size in the nanometer range (15 nm or less). Then, the structural and microstructural effects caused by the use of two carbon source concentrations (2 wt % and 20 wt %) are compared. In the preparation, Ti powders with a hexagonal crystalline structure are considered, along with two carbon sources. The first is stearic acid, with the dual purpose of simultaneously analyzing its effect as a PCA and as a carbon source in TiC formation. The second source is CNTs. The TiC composites were structurally characterized via X-ray diffraction (XRD) and high-resolution transmission electron microscopy (HR-TEM). The microstructure was analyzed via scanning electron microscopy (SEM) and transmission electron microscopy (TEM). Chemical analysis was monitored through energy dispersive X-ray (EDX) mappings, while Raman band analysis complemented the characterization of this material.

2. Experimental Section

2.1. Materials

Combinations of Alpha Aesar titanium powders (Ti, 99.5%) and two different carbon sources (CS) were prepared. Stearic acid (SA) from Sigma-Aldrich Saint Louis, MO, USA ($C_{18}H_{36}O_2$, 95%) and carbon nanotubes (CNTs) synthesized according to the literature [20–22] were utilized as carbon sources (CS). N-heptane from Jalmek (C_7H_{16}, 98.5%) was employed as a process control agent (PCA).

2.2. Synthesis of Nanohybrids Ti-C

Table 1 presents the nomenclature of the titanium and carbon source combinations used at different percentages, 2 and 20 wt % in weight of the elements that compose them [7,23]. The milling process was carried out using an SPEX 800 high-energy mill, with a ball-to-powder ratio of 5:1, and a milling time of 4 h in an argon atmosphere. A total of 1.0 mL of process control agent (n-heptane) was used.

Table 1. The notation used to distinguish the samples with titanium and the different carbon sources employed in the mechanical alloying technique to obtain in situ TiC.

Carbon Sources (CS)	Name	Ti (wt %)	CS (wt %)	Ti (g)	CS (g)
SA	A1	98	2	7.84	0.16
	A2	80	20	6.4	1.6
CNTs	B1	98	2	7.84	0.16
	B2	80	20	6.4	1.6

2.3. Characterization Techniques

The X-ray diffraction (XRD) technique was employed to determine the structure of all the synthesized materials and to ascertain the average crystallite size of the compound. The X-ray diffractometer used was the Panalytical model X'Pert PRO, Almelo, Netherlands. The conditions for obtaining the diffraction patterns were as follows: 2θ (°) in a range of 5–90; step size (○): 0.0131; step time (min): 18. The X-ray diffraction patterns were refined using profile fitting FullProf Suite software [24] (version 2019). The fitting procedure involved the scale factor, zero displacement correction, lattice parameters, background coefficients, pseudo-Voigt peak profile factor, and FWHM [25].

The scanning electron microscopy (SEM) technique was employed to evaluate the morphology, while the chemical composition was monitored using Oxford energy dispersive X-ray (EDX) microanalysis of the samples. SEM micrographs were collected using Hitachi equipment, model SU3500 (Hitachi High-Technologies Corporation, Tokyo, Japan). A voltage of 10 kV was utilized during image collection. The average particle size of the synthesized materials, and their morphologies were monitored using a transmission electron microscope (TEM, model JEOL JEM2200FS, Japan Electron Optics Laboratory Co., Ltd., Tokyo, Japan). Sample preparation for TEM involved dispersing nanoparticles in isopropanol through a sonication process for 1 h. A drop was then deposited onto a Lacey carbon film on a 300 Cu mesh grid.

Raman spectroscopy was utilized to identify the type of carbon allotrope and determine its structural characteristics in the graphitic network. Additionally, it was employed to identify the characteristic bands of TiC. The spectroscope was from Horiba, model LabRam HR Vis-633, with a He-Ne laser source at 632.58 nm. The conditions for obtaining Raman spectra of the samples were as follows: scanning range, 200–1000 cm^{-1}.

3. Results and Discussion

3.1. X-ray Diffraction (XRD) Analysis

In Figure 1, the X-ray diffraction patterns for the powders obtained by the mechanical milling for 4 h are observed. Samples A1 and B1 retain the crystalline structure of the initial titanium phase identified with the crystallographic chart (ICSD 00-044-1294). This

chart is associated with a hexagonal crystalline structure with the Fm-3m (225) space group. The X-ray diffraction pattern of Ti is also included in this figure to compare the diffraction peaks of samples A1 and B1. For sample A2, two broadened signals are observed at 36.56° and 42.32°. The X-ray profile and our indexation are consistent with a previous report by Jia et al., 2009 [7]. According to these authors [7], Ti is gradually consumed due to the formation of TiC with an increasing mechanical alloying time. Therefore, in the XRD pattern of the sample labeled as A2, the presence of a small amount of TiC can be identified. Meanwhile, the X-ray diffraction pattern for sample B2 suggests a majority phase of TiC with the presence of a secondary phase associated with Ti. Suzuki et al., 1995 [16], investigated the formation of metastable intermediate phases that occur after milling Ti hcp and n-heptane in a planetary mill. The authors conducted dry pre-milling for 12 h and wet milling for 20 h (n-heptane), followed by a heat treatment at different temperatures (from 693 K to 1073 K). Their results show the formation of TiC accompanied by a second phase associated with Ti fcc. The authors argue that as the annealing temperature increases, Ti hcp re-emerges. In their interpretation, they suggest that this behavior is reversible. During mechanical milling, the dissolution of C and H occurs. They describe the intermediate phase as a supersaturated solution of C and H. With the increase in temperature, H dissolves, allowing the formation of TiC.
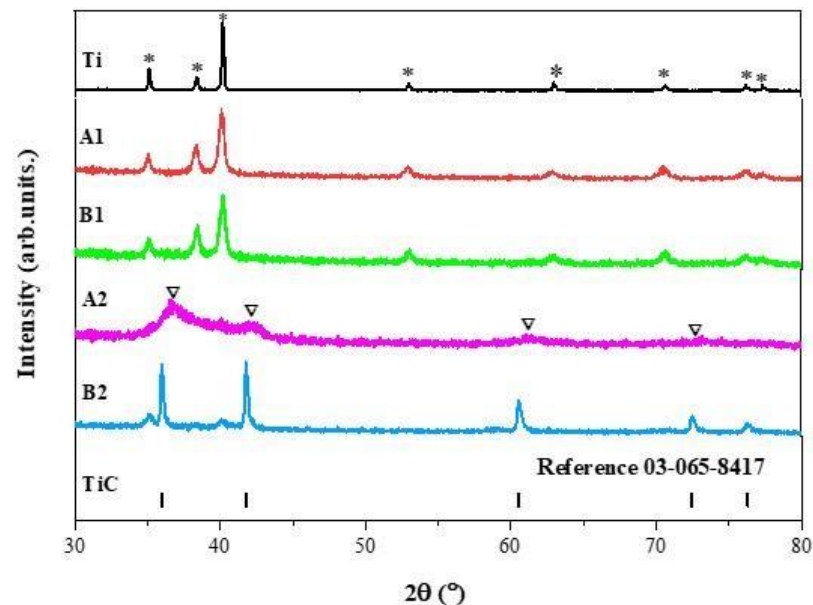
Figure 1. Indexing of X-ray diffraction patterns for samples obtained from milling for 4 h. Samples A1 and B1 demonstrate the formation of Ti (asterisks), whereas sample B2 is predominantly TiC with the presence of Ti. The sample labeled as A2 was indexed considering four peaks (triangles) related to TiC.

The X-ray diffraction patterns of samples A1, B1, and A2 exhibit significantly broadened reflections, which can be attributed to the powders being in the nanoscale range. Subsequently, the average crystallite size was determined using the Scherrer equation with the assistance of X'Pert HighScore software version 2.2b [26].

The results suggest an average crystallite size of 98.4 nm for titanium as powders in the initial stage. After milling, there were achieved reductions of the average crystallite size in samples A1 and B1 of 24.2 nm and 18.7 nm, respectively. For sample B2, an average crystallite size of 34.3 nm was determined. The key conclusions from this analysis include the possibility of a phase transformation from hcp to fcc using the mechanical milling technique, followed by a heat treatment. Additionally, a reduction of the crystallite size was observed.

Bolokang et al., in 2015 [27], mixed Ti hcp with stearic acid at a ratio of 5 wt % for 15 h, followed by sintering and quenching at 1200 °C. In their results, the authors reported sizes of 73 nm for the unmilled titanium and 47 nm after 15 h [28,29]. These results suggest that the combination of liquid and solid process control agents reduces the material's surface tension, favoring a decrease in its size over relatively short milling times.

Rietveld Refinement Method

To determine the parameters of the unit cell in the sample where TiC was predominantly obtained, the refinement of the diffraction patterns was carried out using the Rietveld method implemented using profile fitting FullProf Suite software [24]. Figure 2a presents a comparison between the experimental diffraction pattern (black line with symbols, Y_{obs}) and the calculated diffraction pattern (continuous red line, Y_{calc}). This figure also depicted the residual line (continuous black line, Y_{obs}-Y_{calc}) and Bragg positions for TiC and Ti, respectively.
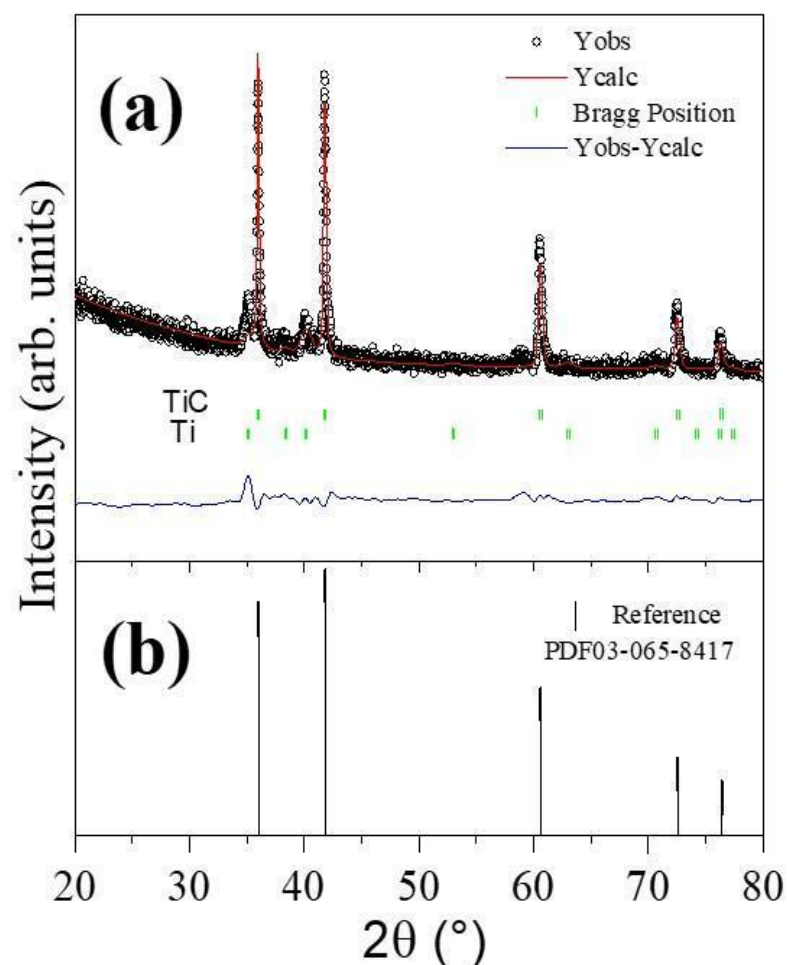
Figure 2. (**a**) Comparison between the experimental diffraction pattern (Y_{obs}) and the refined pattern (Y_{cal}) using the Rietveld method for sample B2. (**b**) Reference pattern for the cubic-type structure similar to NaCl (ICSD 03-065-8417).

The diffraction pattern for sample B2 reveals the presence of two phases, predominantly TiC (cubic, Fm3m space group) and Ti (hexagonal, P6$_3$/mmc space group), which were considered in refinement. The presence of the second phase associated with Ti is a remnant that we considered did not fully react [7,8,30]. The values of the lattice parameter of TiC are in agreement with the data reported in the crystallographic chart ICSD 03-065-8417 (panel b). However, as it can be observed in Table 2, there is a little difference in the lattice volume value. According to T. Kvashina et al. [31] this difference could be attributed

to the partial oxidation of the sample, resulting in the decrease in the average crystallite size and the formation of dislocations stabilized by the impurity oxygen atoms in the crystal lattice of TiC. Table 2 summarizes the refined lattice parameters, volume, and the relative fraction of each component obtained by considering the space groups for TiC and Ti. This table also reports the R factors and the chi-square (χ^2) goodness of fit.

Table 2. The refined lattice parameters, relative fraction of each component, R factors (R_p, R_{wp}, and R_{exp}), volume, and the chi-square (χ^2) goodness of fit obtained by considering the space groups for TiC and Ti. (NA Not available).

Samples	Lattice Parameters	Phase	Relative Fraction	R_p	R_{wp}	R_{exp}	Vol	χ^2
	(Å)		(%)	(%)	(%)	(%)	(Å)^3	
TiC	a = b = c = 4.320(9)	bcc	84.73	17.0	24.1	11.29	80.676	4.54
Ti^{2+}	a = b = 2.951(4) c = 4.688(5)	hcp	15.27				35.371	4.54
Reference ICSD 03-065-8417	a = b = c = 4.320(9)	bcc	100				80.543	NA

3.2. Scanning Electron Microscopy (SEM)

Figure 3a,b shows the SEM features related to the morphology (size, shape, and distribution) of the initial materials (corresponding to the Ti and CNT particles). Additionally, an inset in panel a shows a count of 200 particles to determine the average particle size of the Ti particles. The counting was conducted using the Image J program version 1.50i [32]. The histogram was analyzed employing a log-normal fit using the iterative Levenberg–Marquardt method implemented in the Origin program version 2018 [33].
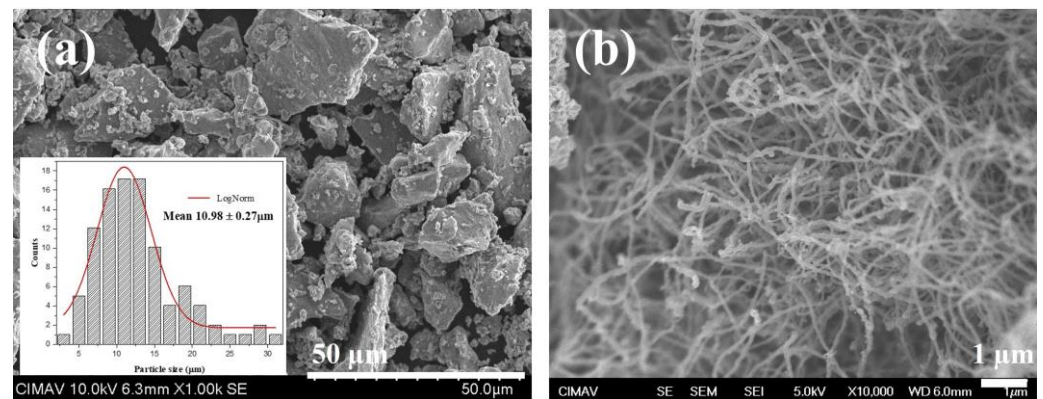
Figure 3. SEM micrographs of starting materials for (**a**) titanium (Ti) particles, and (**b**) carbon nanotubes (CNT). The inset in panel a shows the average particle size obtained by the analysis of the histogram using log-normal fitting.

The morphological features observed in Figure 3a reveal that Ti powders exhibit a non-uniform polygonal shape resembling flakes, with an average particle size of 10.98 ± 0.27 μm. In panel b, a micrograph of CNTs is presented, showcasing their typically long and slender spaghetti-like form, which is prone to clustering.

Figure 4 shows the comparison between the SEM images to monitor the effect of two carbon sources on the size and distribution of the particles used in the formation of TiC. The SEM micrographs for the samples A1 and B1 are depicted at the top of the panel, which contain 2% wt of the carbon sources (SA and CNTs). This micrograph shows that the flake-type shape with a narrow particle distribution predominates (see the yellow arrows). This type of morphology occurs during the AM process between a ductile material (Ti) and a brittle one C. This is due to the multiple fractures and cold welding of the materials, which are caused by the collisions of the mill balls, resulting in a reduction of the size of

the particles. The effect of stearic acid in sample A1 is similar to the NTCs. They acted as a lubricant when adhered to the surface of the metal (Ti) and inhibited the cold welding of the particles.
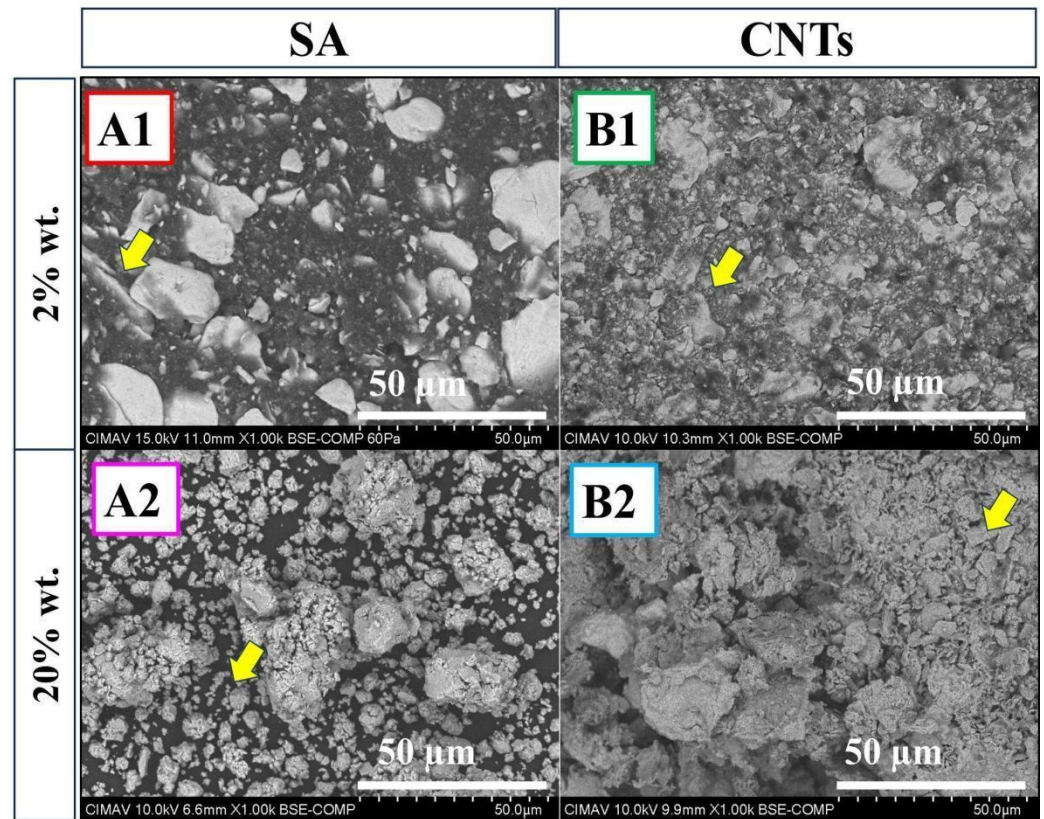
Figure 4. Comparison between SEM micrographs that show the morphological behavior of (**A1**–**B2**) powders prepared via mechanical alloying TiC. For (**A1**,**B1**) samples, flake-type shape is observed (yellow arrows), while (**A2**,**B2**) samples exhibit agglomerated flake-type particles.

The SEM micrographs for the samples A2 and B2 are shown at the bottom of the panel, with a carbon content of 20 wt %. In sample A2, irregularly shaped particles smaller than 10 μm are observed, while in sample B2, finer flake-like shapes predominate. Both samples show the presence of the TiC phase (Figure 1). In the literature [34,35], it has been reported that during MA, ductile Ti particles envelop brittle particles, in this case, C. When the balance between fracturing and cold welding is lost, the agglomerate size grows due to the high surface energy produced on the new surface. This new surface results from particle fracturing, compressing, and increasing intimate contact between the atoms, accelerating C diffusion into titanium, and inducing forging work [34,35].

In Figure 4, sample A2, the combination of 20 wt % stearic acid and n-heptane has a dual effect: (i) acting as a lubricant (ii) when welding dominates over the fracture. This phenomenon is attributed to the decomposition of stearic acid, and n-heptane, during this stage, acts as a carbon source, leading to a TiC-deficient phase, as observed in Figure 1. Conversely, for sample B2 with 20 wt % CNTs, in the first stage, the CNTs and n-heptane act as lubricants, reducing the particle size. Milling generates interstitial defects and dislocations in both materials, increasing their chemical reactivity. In this stage, the CNTs are introduced into the Ti layers, and as the temperature rises during milling, TiC formation occurs. If the temperature decreases, it can be attributed to the partial transformation of reactants, developing intimate contact between the CNTs and Ti [36,37].

Elemental Microanalysis—EDS Elemental Mapping

During mechanical alloying, there is a possibility of powder contamination occurring due to the milling conditions or interstitial impurities present in the air within the vial (nitrogen and oxygen). The estimation of the atomic percentages of Ti, C, and the presence of O may be due to exposure to the environment, leading to the absorption of oxygen species like hydroxyl species (OH^-) and O^- ions. Another potential cause is the components of the PCA when used in high quantities during milling [13,38]. All the metals are inherently reactive and can easily combine with elements, such as hydrogen, oxygen, carbon, and nitrogen, to form hydrides, oxides, carbides, and nitrides [39].

In Figure 5, the SEM-EDS elemental maps of samples A1 and B1 are shown, revealing a uniform chemical distribution. The results suggest that these elements are not present at the interstitial sites or in the form of oxides or carbides. In sample A2, the absence of C is observed, possibly because it was embedded within the Ti layers. Conversely, in sample B2, the distribution of elements indicates the formation of the TiC phase, as evidenced via XRD analysis (Figure 1).
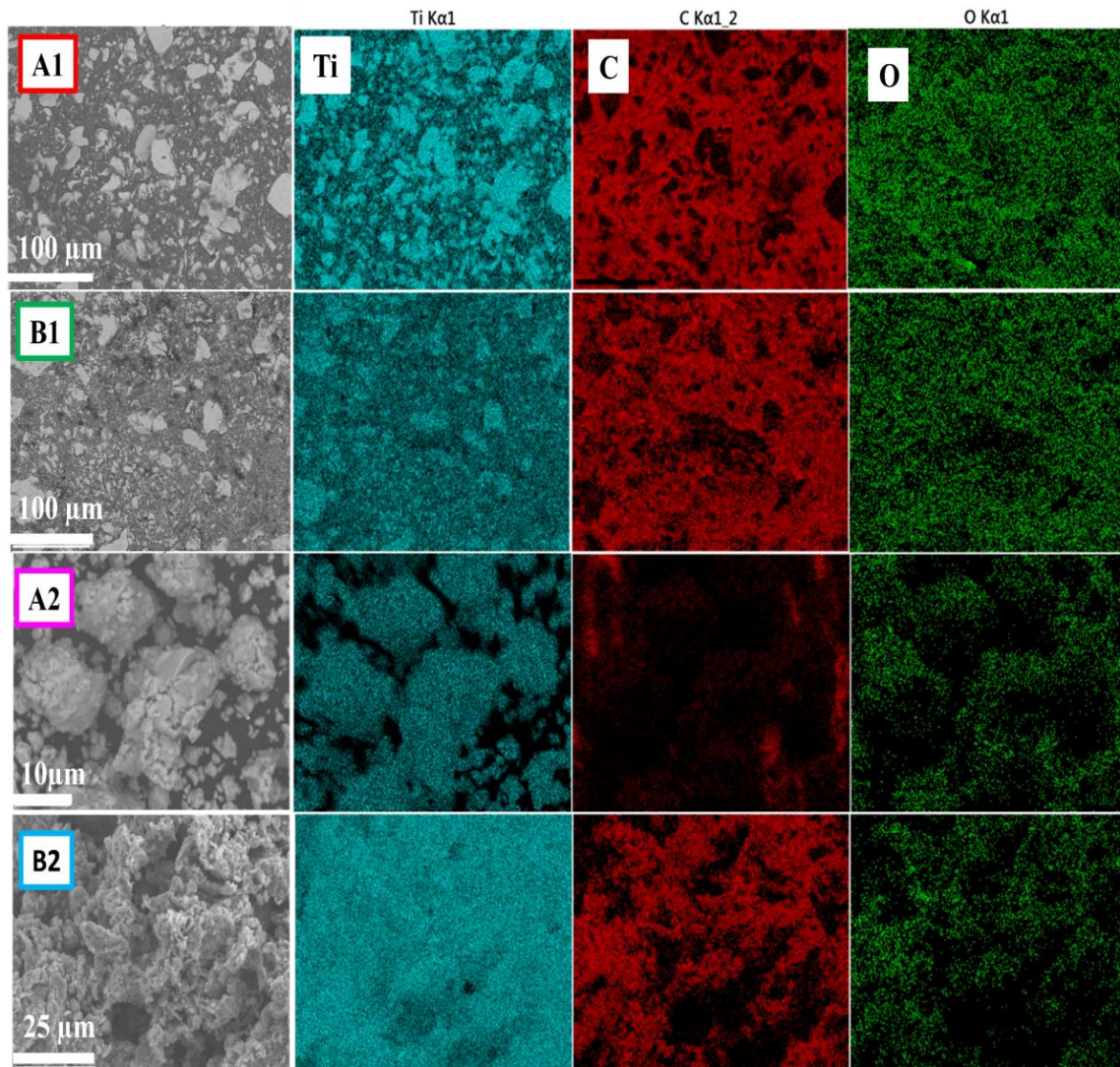
Figure 5. Comparison between SEM-EDS map of element distribution (titanium, oxygen, and carbon) in the alloy powders TiC. (**A1,A2**) samples are prepared with SA, while (**B1,B2**) are obtained with CNTs.

3.3. High-Resolution Transmission Electron Microscopy (HR-TEM)

Figure 6 presents the HR-TEM micrographs of sample B2, which predominantly exhibits the TiC phase. HR-TEM analysis provides information on the morphology, structure, and size of the particles. In Figure 6a, a CNT with a section showing defects (yellow square), possibly due to the milling process, is observed. Additionally, a framework structure composed of TiC particles can be seen. This type of formation is similar to that described by Saba et al. in 2017 [28]. In their study, they explain two possible sources of carbon when using CNTs for TiC synthesis: (i) defects in the CNT walls, and (ii) deformed parts detached from the CNT walls. Figure 6b is a schematic visualization containing both the mechanisms for the formation of TiC nanocrystals. This visualization was created using VESTA software, version 3.4.6 [40]. The arrows indicate the direction of the Ti particles reacting with the CNT walls, forming nanoblocks around them. During milling, Ti particles are introduced into the CNTs, mainly at the ends containing defects [9,17].
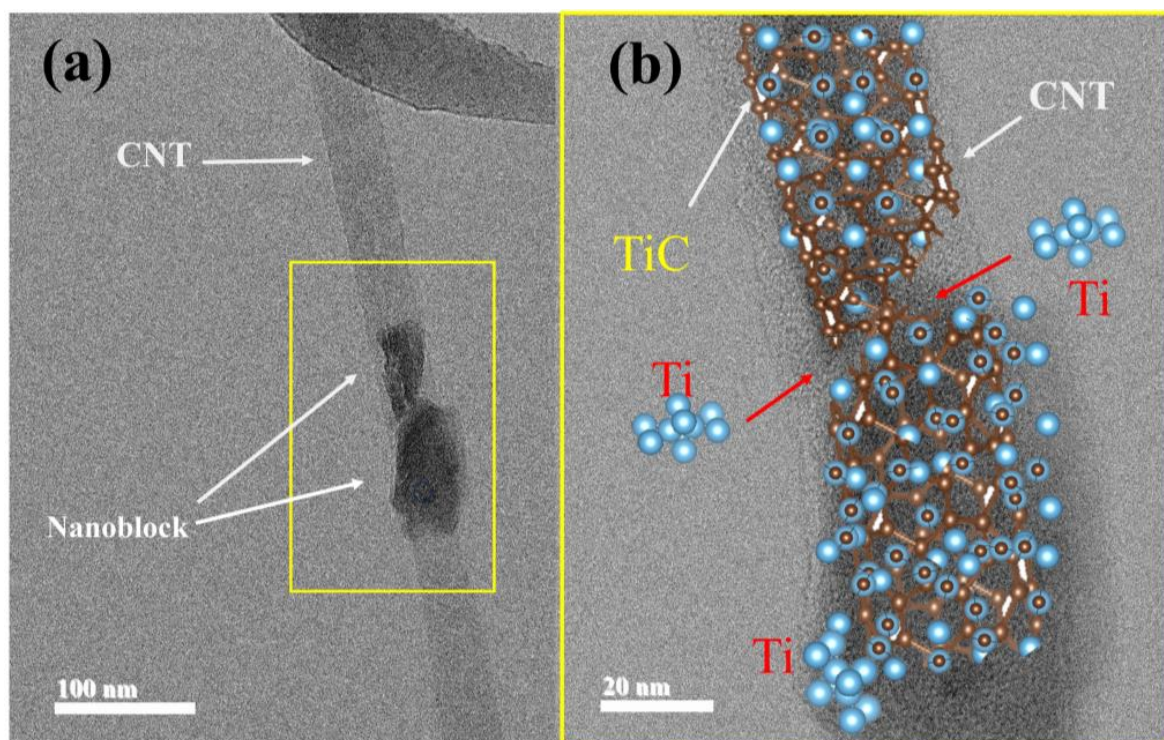
Figure 6. HR-TEM micrographs of CNT with TiC. (**a**) Nanoblock of TiC developed in a CNT, and (**b**) schematic visualization of the formation mechanism of in situ TiC around a CNT using VESTA software, version 3.

Continuing with the microstructural analysis of the TiC nanoparticles, Figure 7a presents a representative HR-TEM micrograph. In this micrograph, two highlighted regions can be observed. The first region marked in blue shows two polygonal-shaped particles merging to form a lump-like structure [28], corresponding to TiC. In the second region marked in yellow, an elongated microstructure corresponding to the CNTs can be observed. Figure 7b provides a magnification of a CNT section, indexed using Digital Micrograph software, version 3.6.1 [41] and the identification card, ICSD 00-041-1487. Indexing associates an interplanar distance of 0.34 nm with the (0 0 2) plane. Figure 7c shows a section within the polygonal particle, where a distance of 0.245 nm corresponding to the (1 1 1) plane of TiC was obtained, with the identification card, ICSD 03-065-8417. Dislocations and folded zones resulting from milling, indicating a plastically deformed structure, can also be observed within the image. It is worth noting the indexed regions in the high-resolution images exhibit crystallinity that persists after the 4 h milling process.
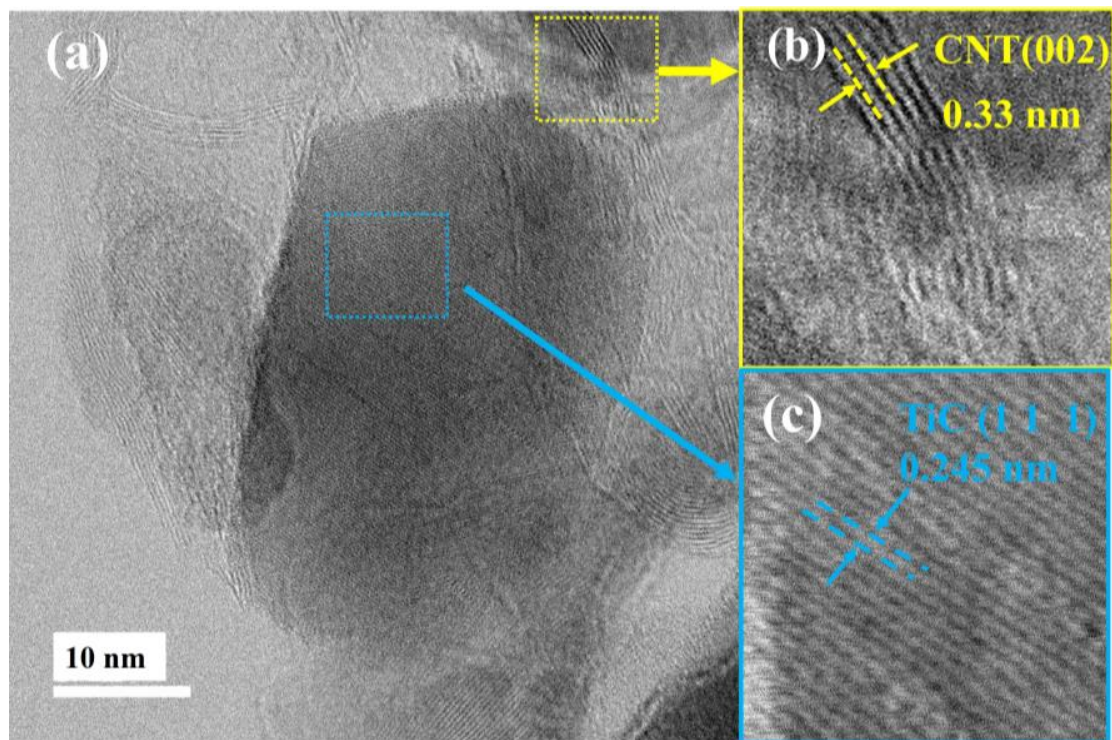
Figure 7. (**a**) cHR-TEM image of TiC (sample B2). Indexing of interplanar distances. (**b**) FFT image corresponding to CNT (yellow box). (**c**) FFT image corresponding to TiC (blue box).

3.4. Raman Spectroscopy Analysis

Raman spectroscopy was employed to assess the effect of milling on the structure of CNTs and evaluate the influence of carbon sources on TiC formation. Titanium, like most metals, does not exhibit active vibration modes. On the other hand, CNTs, like all carbon allotropes, show two main bands named D and G. The D band is associated with the concentration of defects or a measure of disorder in C-C bonds within the graphitic network, while the G band is associated with in-plane vibrations of the C-C bonds and the degree of graphitization or metallicity of graphitic materials [42,43].

Figure 8 contains the Raman spectra of the samples. The Raman spectra can be divided into two regions for this description. In the first region (from 200–1000 cm^{-1}), three Raman bands associated with the Ti-C bond are observed. These peaks centered at 220, 420, and 605 cm^{-1} are comparable to those reported in the literature [44,45]. In the second region (from 1000 to 2000 cm^{-1}), the sample B2 with 20 wt % CNTs exhibits the most intense signals. Regarding the signals from non-reacted carbon, both the D and G signals are detected at 1320 and 1590 cm^{-1}, respectively. These signals are associated with the A_{1g} and E_{2g} vibrational modes of graphitic structures. They are present with low-level intensity on panels (a, c and d). It is characteristic of high-energy milling that, when milling graphitic compounds like CNTs, the milling process destroys the ordered structure present. This leads to an increase in the intensity of the D band [46].
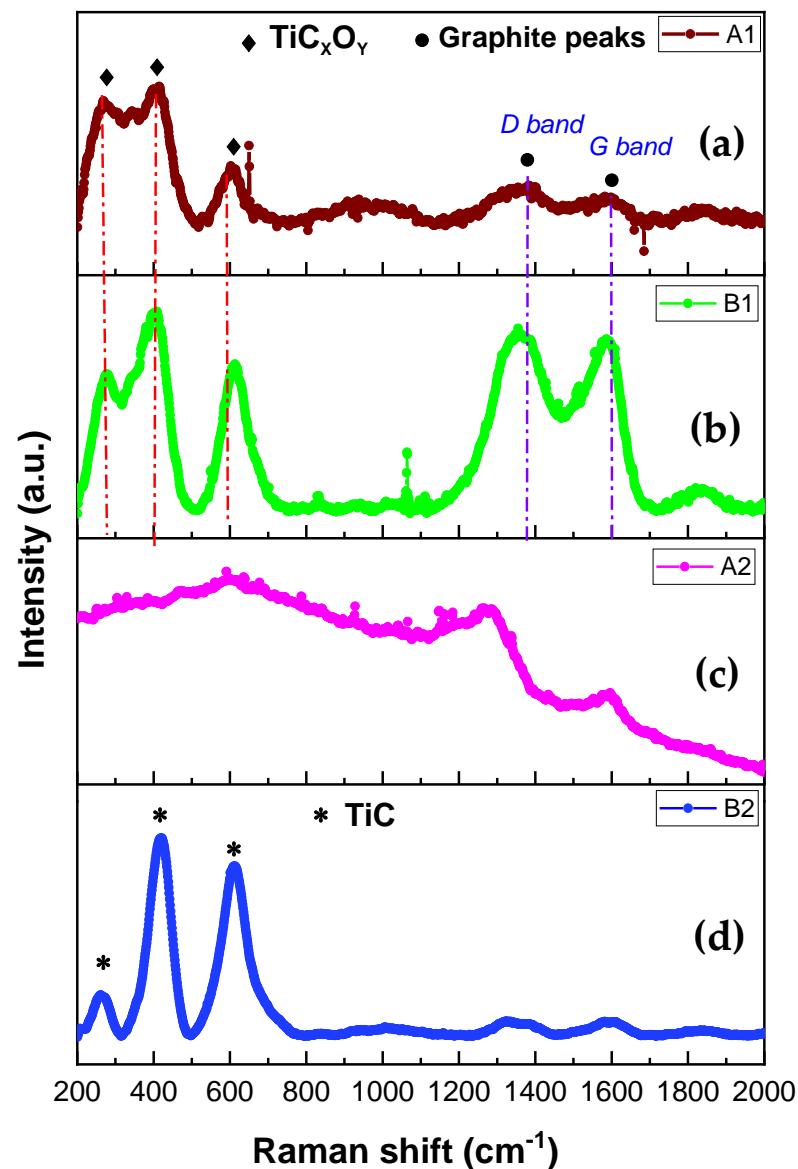
Figure 8. Raman spectra of Ti and C powders milled. Panels (**a**,**c**) are related to A1 and A2 samples prepared with SA. Panels (**b**,**d**) exhibit the profile for B1 and B2 samples prepared with CNTs. The label TiCxOy is associated with titanium oxycarbide (diamonds dash-dot line), and TiC is titanium carbide (asterisks). Graphite peaks are denoted as D and G bands (circles and violet dash–dot line).

Sample A1 (panel a), which contains 2 wt % SA, reveals broad and low-intensity peaks, contrary to sample B1 (panel b) with 2 wt % CNTs, which shows high-intensity-level peaks for both bands. In the first region, it can be noticed Raman signals attributed to the presence of titanium oxycarbide (TiC_xO_y). In the second region, we identified the graphite signals [46]. These results align with the XRD analysis, where only Ti was identified. Sample A2 (panel c) with a 20 wt % SA content contains broad and poorly defined peaks, indicating deficient crystalline synthesis.

Samples synthesized with stearic acid show less definition in the signals, both for TiC and the remaining carbon. The sample with 20 wt % (panel d). CNTs are the ones where TiC signals are observed with greater definition, consequently indicating a higher synthesis yield.

4. Conclusions

In summary, the optimization of the in situ formation of TiC nanoparticles through a simple and scalable synthesis using mechanical alloying with two different carbon sources (stearic acid and carbon nanotubes) was performed. The self-propagation reaction between Ti and C developed in a short time of 4 h. XRD analysis using the Rietveld method confirmed the formation of TiC with an fcc structure. The peak broadening analysis suggests average crystallite sizes of 15.15 nm and 9.45 nm, respectively. With 2 wt % of stearic acid or carbon nanotubes, it induces the formation of thin flake-type shape particles. For the composites with 20 wt % of stearic acid or carbon nanotubes, the particles exhibit a quasi-round shape that tends to aggregate forming clusters. The effect of solid and liquid PCA contributes to reducing the particle size in the A1 and B1 samples. However, for the A2 and B2 samples, 20 wt % of stearic acid or carbon nanotubes is required to consolidate the TiC phase. The tendency for TiC nanoparticles to develop nanoblocks and nanolump-type shapes on the surface and fragmented parts of the nanotubes was observed for B2. Raman spectroscopy analysis indicates the higher synthesis yield of TiC in sample B2 due to the carbon source reacting almost entirely. This result agrees with the XRD analysis, quantifying 84.57% of the TiC phase using the Rietveld method. This work provides an effective approach to obtain carbides using carbon nanotubes with smaller crystal sizes.

Author Contributions: Conceptualization, M.L.C.-R. and G.H.-P.; methodology, D.L.-G.; software, J.E.G.-H. and J.A.B.-C.; validation, D.L.-G. and R.P.-B.; formal analysis, M.L.C.-R.; investigation, M.L.C.-R.; resources, G.H.-P.; data curation, M.A.R.E.-R.; writing—original draft preparation, M.L.C.-R.; writing—review and editing, G.H.-P. and M.L.C.-R.; visualization, D.L.-G.; supervision, D.L.-G. All authors have read and agreed to the published version of the manuscript.

Data Availability Statement: Data are contained within the article.

Conflicts of Interest: The authors declare no conflict of interest.

References

1. Dong, B.X.; Qiu, F.; Li, Q.; Shu, S.L.; Yang, H.Y.; Jiang, Q.C. The Synthesis, Structure, Morphology Characterizations and Evolution Mechanisms of Nanosized Titanium Carbides and Their Further Applications. *Nanomaterials* **2019**, *9*, 1152. [CrossRef] [PubMed]
2. Rao, V.R.; Ramanaiah, N.; Sarcar, M.M.M. Tribological properties of Aluminium Metal Matrix Composites (AA7075 Reinforced with Titanium Carbide (TiC) Particles). *Int. J. Adv. Sci. Technol.* **2016**, *88*, 13–26. [CrossRef]
3. He, B.; Ma, D.; Ma, F.; Xu, K. Microstructures and wear properties of TiC coating produced by laser cladding on Ti-6Al-4V with TiC and carbon nanotube mixed powders. *Ferroelectrics* **2019**, *547*, 217–225. [CrossRef]
4. Cochepin, B.; Gauthier, V.; Vrel, D.; Dubois, S. Crystal growth of TiC grains during SHS reactions. *J. Cryst. Growth* **2007**, *304*, 481–486. [CrossRef]
5. Zhang, L.; Hu, J.; Voevodin, A.A.; Fong, H. Synthesis of continuous TiC nanofibers and/or nanoribbons through electrospinning followed by carbothermal reduction. *Nanoscale* **2010**, *2*, 1670–1673. [CrossRef] [PubMed]
6. Suryanarayana, C.; Ivanov, E. Mechanochemical synthesis of nanocrystalline metal powders. Woodhead Publishing Series in Metals and Surface Engineering. In *Advances in Powder Metallurgy*; Woodhead Publishing: Sawston, UK, 2013; pp. 42–68.
7. Jia, H.; Zhang, Z.; Qi, Z.; Liu, G.; Bian, X. Formation of nanocrystalline TiC from titanium and different carbon sources by mechanical alloying. *J. Alloys Compd.* **2009**, *472*, 97–103. [CrossRef]
8. Lohse, B.H.; Calka, A.; Wexler, D. Synthesis of TiC by controlled ball milling of titanium and carbon. *J. Mater. Sci.* **2006**, *42*, 669–675. [CrossRef]
9. Korchagin, M.A.; Gabdrashova, S.E.; Dudina, D.V.; Bokhonov, B.B.; Bulina, N.V.; Kuznetsov, V.L.; Ishchenko, A.V. Combustion characteristics and structure of carbon nanotube/titanium composites. *J. Therm. Anal. Calorim.* **2019**, *137*, 1903–1910. [CrossRef]

10. Nouri, A.; Wen, C. Surfactants in Mechanical Alloying/Milling: A Catch-22 Situation. *Crit. Rev. Solid State Mater. Sci.* **2013**, *39*, 81–108. [CrossRef]

11. Alamolhoda, S.; Heshmati-Manesh, S.; Ataie, A.; Badiei, A. Role of process control agents on milling behavior of Al and TiO$_2$ powder mixture to synthesize TiAl/Al$_2$O$_3$ nano composite. *Int. J. Mod. Phys. Conf.* **2012**, *5*, 638–645. [CrossRef]

12. Tokumitsu, K. Reduction of metal oxides by mechanical alloying method. *Solid State Ion.* **1997**, *101–103*, 25–31.

13. Nouri, A.; Hodgson, P.D.; Wen, C.E. Study on the Role of Stearic Acid and Ethylene-bis-stearamide on the Mechanical Alloying of a Biomedical Titanium Based Alloy. *Metall. Mater. Trans. A* **2010**, *41*, 1409–1420. [CrossRef]

14. Schoenitz, M.; Zhu, X.; Dreizin, E.L. Carbide formation in Al–Ti mechanical alloys. *Scr. Mater.* **2005**, *53*, 1095–1099. [CrossRef]

15. Jari Keskinen, A.P.; Rubin, J.; Ruuskanen, P. Carbide and hydride formation during mechanical alloying of titanium and aluminium with hexane. *Mater. Sci. Eng. A* **1995**, *196*, 205–211. [CrossRef]

16. Suzuki, T.S.; Nagumo, M. Metaestable intermediate phase formation at reaction milling of titanium and n-Heptane. *Scr. Metall. Mater.* **1995**, *32*, 1215–1220. [CrossRef]

17. Liu, Z.G.; Guo, J.T.; Ye, L.L.; Li, G.S.; Hu, Z.Q. Formation mechanism of TiC by mechanical alloying. *Appl. Phys. Lett.* **1994**, *65*, 2666–2668. [CrossRef]

18. Ye, L.L.; Quan, M.X. Synthesis of nanocrystalline TiC powders by mechanical alloying. *Nanostruct. Mater.* **1995**, *5*, 25–31. [CrossRef]

19. Schaffer, G.B.; Forrester, J.S. Influence of collision energy and strain accumulation on the kinetics of mechanical alloying. *J. Mater. Sci.* **1997**, *32*, 3157–3162. [CrossRef]

20. Aguilar-Elguézabal, A.; Antúnez, W.; Alonso, G.; Delgado, F.P.; Espinosa, F.; Miki-Yoshida, M. Study of carbon nanotubes synthesis by spray pyrolysis and model of growth. *Diam. Relat. Mater.* **2006**, *15*, 1329–1335. [CrossRef]

21. Valenzuela-Muñiz, A.M.; Alonso-Nuñez, G.; Miki-Yoshida, M.; Botte, G.G.; Verde-Gómez, Y. High electroactivity performance in Pt/MWCNT and PtNi/MWCNT electrocatalysts. *Int. J. Hydrogen Energy* **2013**, *38*, 12640–12647. [CrossRef]

22. Rosado, G.; Verde, Y.; Valenzuela-Muñiz, A.M.; Barbosa, R.; Miki Yoshida, M.; Escobar, B. Catalytic activity of Pt-Ni nanoparticles supported on multi-walled carbon nanotubes for the oxygen reduction reaction. *Int. J. Hydrogen Energy* **2016**, *41*, 23260–23271. [CrossRef]

23. Gao, Y.Y.; Qiu, F.; Liu, T.S.; Chu, J.G.; Zhao, Q.L.; Jiang, Q.C. Effects of Carbon Source on TiC Particles' Distribution, Tensile, and Abrasive Wear Properties of In Situ TiC/Al-Cu Nanocomposites Prepared in the Al-Ti-C System. *Nanomaterials* **2018**, *8*, 610. [CrossRef] [PubMed]

24. Rodriguez-Carbajal, J. Recent advances in magnetic structure determination by neutron powder diffraction. *Phys. B Condens. Matter.* **1993**, *192*, 55–69. [CrossRef]

25. McCusker, L.B.; Von Dreele, R.B.; Cox, D.E.; Louer, D.; Scardi, P. Rietveld refinement guidelines. *J. Appl. Crystallogr.* **1999**, *32*, 36–50. [CrossRef]

26. Degen, T.; Sadki, M.; Bron, E.; König, U.; Nénert, G. The HighScore suite. *Difracción De Polvo* **2014**, *29*, S13–S18. [CrossRef]

27. Bolokang, A.S.; Motaung, D.E.; Arendse, C.J.; Muller, T.F.G. Formation of the metastable FCC phase by ball milling and annealing of titanium–stearic acid powder. *Adv. Powder Technol.* **2015**, *26*, 632–639. [CrossRef]

28. Saba, F.; Sajjadi, S.A.; Haddad-Sabzevar, M.; Zhang, F. Formation mechanism of nano titanium carbide on multi-walled carbon nanotube and influence of the nanocarbides on the load-bearing contribution of the nanotubes inner-walls in aluminum-matrix composites. *Carbon* **2017**, *115*, 720–729. [CrossRef]

29. Yan, M.; Qian, M.; Kong, C.; Dargusch, M.S. Impacts of trace carbon on the microstructure of as-sintered biomedical Ti-15Mo alloy and reassessment of the maximum carbon limit. *Acta Biomater.* **2014**, *10*, 1014–1023. [CrossRef]

30. Munir, K.S.; Li, Y.; Liang, D.; Qian, M.; Xu, W.; Wen, C. Effect of dispersion method on the deterioration, interfacial interactions and re-agglomeration of carbon nanotubes in titanium metal matrix composites. *Mater. Des.* **2015**, *88*, 138–148. [CrossRef]

31. Kvashina, T.; Uvarov, N.; Ukhina, A. Synthesis of Titanium Carbide by Means of Pressureless Sintering. *Ceramics* **2020**, *3*, 306–311. [CrossRef]

32. Schneider, C.; Rasband, W.; Eliceiri, K. NIH Image to ImageJ: 25 years of image analysis. *Nat. Methods* **2012**, *9*, 671–675. [CrossRef] [PubMed]

33. *Origin(Pro), Version 2018*; OriginLab Corporation: Northampton, MA, USA, 2018.

34. Yuan, Q.; Zheng, Y.; Yu, H. Synthesis of nanocrystalline Ti(C, N) powders by mechanical alloying and influence of alloying elements on the reaction. *Int. J. Refract. Met. Hard Mater.* **2009**, *27*, 121–125. [CrossRef]

35. Rahaei, M.B.; Yazdani rad, R.; Kazemzadeh, A.; Ebadzadeh, T. Mechanochemical synthesis of nano TiC powder by mechanical milling of titanium and graphite powders. *Powder Technol.* **2012**, *217*, 369–376. [CrossRef]

36. Adegbenjo, A.O.; Olubambi, P.A.; Potgieter, J.H.; Nsiah-Baafi, E.; Shongwe, M.B. Interfacial Reaction During High Energy Ball Milling Dispersion of Carbon Nanotubes into Ti$_6$Al$_4$V. *J. Mater. Eng. Perform.* **2017**, *26*, 6047–6056. [CrossRef]

37. Munir, K.S.; Li, Y.; Qian, M.; Wen, C. Identifying and understanding the effect of milling energy on the synthesis of carbon nanotubes reinforced titanium metal matrix composites. *Carbon* **2016**, *99*, 384–397. [CrossRef]

38. Dorofeev, G.A.; Lubnin, A.N.; Lad'yanov, V.I.; Mukhgalin, V.V.; Puskkarev, B.E. Structural and phase transformations during ball milling of titanium in medium of liquid hydrocarbons. *Phys. Met. Metallogr.* **2014**, *115*, 157–168. [CrossRef]

39. Seelam, U.M.R.; Barkhordarian, G.; Suryanarayana, C. Is there a hexagonal-close-packed (hcp)→face-centered-cubic (fcc) allotropic transformation in mechanically milled Group IVB elements? *J. Mater. Res.* **2011**, *24*, 3454–3461. [CrossRef]

40. Momma, K.; Izumi, F. VESTA: A three-dimensional visualization system for electronic and structural analysis. *J. Appl. Crystallogr.* **2008**, *41*, 653–658. [CrossRef]

41. Mitchell, D.R.; Shaffer, B. Scripting-customized microscopy tools for Digital Micrograph. *Ultramicroscopy* **2005**, *103*, 319–332. [CrossRef]

42. Lehman, J.H.; Terrones, M.; Mansfield, E.; Hurst, K.E.; Meunier, V. Evaluating the characteristics of multiwall carbon nanotubes. *Carbon* **2011**, *49*, 2581–2602. [CrossRef]

43. Delhaes, P.; Couzi, M.; Trinquecoste, M.; Dentzer, J.; Hamidou, H.; Vix-Guterl, C. A comparison between Raman spectroscopy and surface characterizations of multiwall carbon nanotubes. *Carbon* **2006**, *44*, 3005–3013. [CrossRef]

44. Klein, M.V.; Holy, J.A.; Williams, W.S. Raman scattering induced by carbon vacancies in TiC_x. *Phys. Rev. B* **1978**, *17*, 1546–1556. [CrossRef]

45. Amer, M.; Barsoum, M.W.; El-Raghy, T.; Weiss, I.; Leclair, S.; Liptak, D. The Raman spectrum of Ti_3SiC_2. *J. Appl. Phys.* **1998**, *84*, 5817–5819. [CrossRef]

46. Magnus, C.; Sharp, J.; Rainforth, W.M. The Lubricating Properties of Spark Plasma Sintered (SPS) Ti_3SiC_2 MAX Phase Compound and Composite. *Tribol. Trans.* **2019**, *63*, 38–51. [CrossRef]